

Quantum Sensing in Tweezer Arrays: Optical Magnetometry on an Individual-Atom Sensor Grid

Dominik Schöffner,¹ Tobias Schreiber,¹ Fabian Lenz,¹ Malte Schlosser,¹ and Gerhard Birkel^{1,2,*}

¹*Technische Universität Darmstadt, Institut für Angewandte Physik,
Schlossgartenstraße 7, 64289 Darmstadt, Germany*

²*Helmholtz Forschungsakademie Hessen für FAIR (HFHF),
Campus Darmstadt, Schlossgartenstraße 2, 64289 Darmstadt, Germany*

(Dated: July 18, 2023)

We implemented a scalable platform for quantum sensing comprising hundreds of sites capable of holding individual laser-cooled atoms and demonstrate the applicability of this single-quantum-system sensor array to magnetic-field mapping on a two-dimensional grid. With each atom being confined in an optical tweezer within an area of $0.5\ \mu\text{m}^2$ at mutual separations of $7.0(2)\ \mu\text{m}$, we obtain micrometer-scale spatial resolution and highly parallelized operation. An additional steerable optical tweezer allows for a rearrangement of atoms within the grid and enables single-atom scanning microscopy with sub-micron resolution. Our novel individual-atom sensor platform finds its immediate application in mapping an externally applied DC gradient magnetic field. In a Ramsey-type measurement, we obtain a field resolution of $98(29)\ \text{nT}$. A calculation based on the net time of coherent evolution leads to a sensitivity of $20(7)\ \text{nT}/\sqrt{\text{Hz}}$.

The paradigm of exploiting quantum properties of physical systems for sensing purposes has paved the way to devices with unprecedented sensitivity that outshine their classical counterparts [1, 2]. The fact that energy levels of quantum systems in general are susceptible to their environment allows for measuring, e.g., external electric or magnetic fields. In this context, devices based on superconducting circuits [3–6], nitrogen-vacancy centers [7–10], and optically pumped atomic magnetometers [11–13] have been developed to highly sensitive systems for magnetic-field sensing. Each approach exhibits a specific set of advantages and limitations due to its characteristics derived from the physical properties when benchmarked with respect to sensitivity, spatial resolution, field of view, or ambient conditions - to name only a few crucial parameters.

In recent years, this technological toolbox has been enriched by methods based on ultracold neutral-atom quantum systems. Localized atom clouds represent well-controllable sensors combining high-precision measurements with micrometer-scale spatial resolution and millimeter-scale measurement regions. Building on miniaturized magnetic traps, ultracold-atom magnetic-field microscopy renders the simultaneous observation of microscopic and macroscopic effects possible [14, 15]. Optical dipole traps establish a basis for sensors that are detached from any perturbing surface, thereby facilitating high-precision all-optical magnetometers [16–19] whose sensitivity has been further amplified by entanglement-enhanced measurements [20, 21]. In addition to magnetic-field mapping, further applications include the rectification of the magnetic field environment for neutral-atom quantum science. This has been demon-

strated by counteracting on global fluctuations in Bose-Einstein condensates [18] and error mitigation in quantum simulation and computing [19, 22]. In particular, optical tweezer arrays [23] facilitate spatially configurable quantum sensing in a scalable fashion.

We report on the realization of an individual-atom magnetic-field sensor grid in a highly scalable architecture. Individual neutral atoms are loaded into microlens-generated tweezers [24, 25] with micrometer-sized pitch for the measurement of the ambient magnetic field. We use this sensor array to map an externally applied magnetic gradient field. An auxiliary transport tweezer is utilized to increase the duty cycle by maintaining a high atom number within a sub-array for local measurements. In addition, this steerable tweezer increases the spatial resolution as an individual probe decoupled from the array grid. While already providing hundreds of sensor pixels in 2D in this work, our platform is intrinsically scalable to 3D arrays with thousands of sensor atoms as presented in Ref. [26].

We realize magnetic-field sensing in the neutral-atom platform that is described in detail in Refs. [25, 27] and schematically illustrated in Fig. 1(a). Created by micro-fabricated optical elements, this setup constitutes a two-dimensional focused-beam optical dipole trap array, i.e., tweezer array, for the parallelized, site-resolved control of single-atom quantum systems. The tweezer spacing is $7.0(2)\ \mu\text{m}$ and the tweezer waist is $1.45(10)\ \mu\text{m}$. Throughout this article, uncertainties are given as 1σ statistical uncertainties. The tweezers are loaded with laser-cooled ^{85}Rb atoms. Due to light-assisted collisions each site is either empty or occupied by one atom at most (see Refs. [23, 28] and references therein), resulting in a typical loading efficiency of 50%. From the known values of potential depth ($U = k_B \times 0.2\ \text{mK}$) and temperature ($52\ \mu\text{K}$), we infer a 2D spatial localization of each atom of $0.5\ \mu\text{m}^2$. Covering an area of 18×15 sites

* Contact for correspondence: apqpub@physik.tu-darmstadt.de;
<https://www.iap.tu-darmstadt.de/apq>

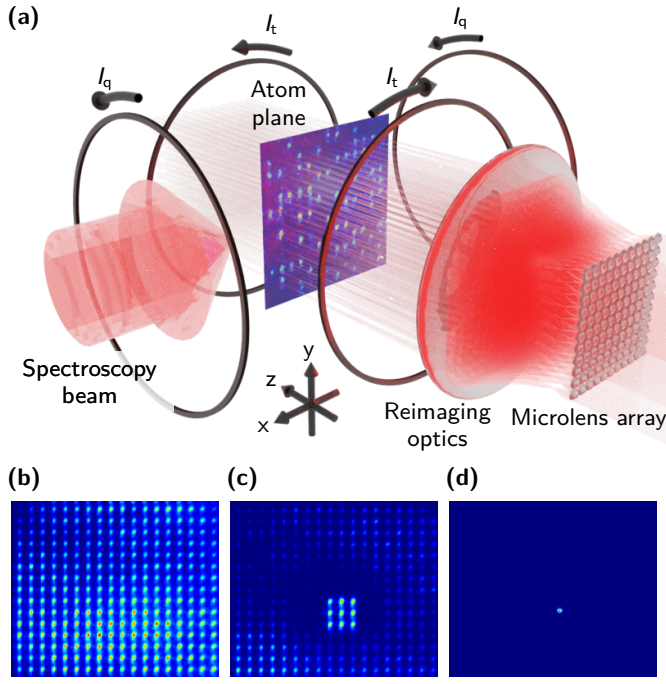


FIG. 1: Micro-optical tweezer array for cold-atom magnetometry. (a) Schematic experimental setup. A 270-site single-atom register is generated by a microlens array whose focal plane is reimaged into the vacuum chamber (typical parameters: trapping wavelength $\lambda = 797$ nm, trap depth $U = k_B \times 1$ mK). Two-photon Ramsey spectroscopy is used to characterize the magnetic-gradient test field induced by the two anti-Helmholtz coils with counterpropagating current I_t . A pair of coils in Helmholtz configuration provides a well-defined quantization axis via a homogeneous field generated by a current I_q . (b) Averaged fluorescence of atoms in the 18×15 tweezer array. (c) Enhanced atom occupation in a pre-defined sub-structure using a steerable optical tweezer for atom transport. (d) Using solely the steerable tweezer, atoms can be positioned independently of the array grid.

($119 \mu\text{m} \times 98 \mu\text{m}$), this configuration serves as planar sensor grid for magnetic-field mapping. Our setup includes an additional movable optical tweezer with a waist of $2.0(1) \mu\text{m}$ that can be used to arrange the randomly loaded atoms in predefined geometries. Site-resolved fluorescence detection of the atoms is realized through excitation at the rubidium D2-line and imaging the atom plane onto an electron-multiplying charge-coupled device (EMCCD) camera within an exposure time of 60 ms. Figure 1(b) shows an averaged fluorescence image of atoms in the full sensor region while in Fig. 1(c) the enhanced atom occupation in a 3×3 pre-defined target structure after rearrangement is depicted. Fig. 1(d) shows the fluorescence of single atoms loaded into the steerable optical tweezer.

The spectroscopy beam in Fig. 1(a) drives a two-photon transition between the long-lived hyperfine

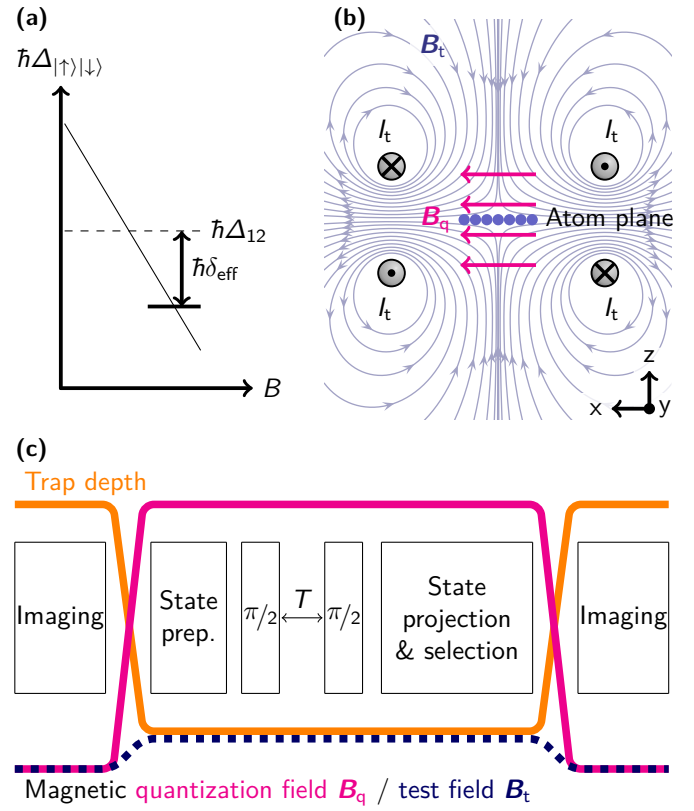


FIG. 2: Experimental details of individual-atom magnetometry. (a) Energy splitting $\hbar\Delta_{|\uparrow\rangle|\downarrow\rangle}$ of the two states $|\uparrow\rangle$ and $|\downarrow\rangle$ used for magnetic field sensing as a function of the field strength. For a fixed differential two-photon energy $\hbar\Delta_{12}$ of the spectroscopy beam (dashed horizontal line), the effective detuning δ_{eff} depends on the magnetic field experienced by the atom. (b) The inhomogeneous magnetic field B_t generated by a pair of coils in anti-Helmholtz configuration is used as a position-dependent test field. A homogeneous magnetic field B_q defines the quantization axis. (c) Schematic illustration of a typical measurement cycle (see text for details). During the Ramsey sequence, consisting of state preparation, $\pi/2$ pulse, free precession, $\pi/2$ pulse, and state projection & selection, the trap depth is $U = k_B \times 0.2$ mK whereas for initial atom loading and the two imaging sequences $U = k_B \times 1$ mK.

ground states $|\uparrow\rangle = |5S_{1/2}, F = 3, m_F = -1\rangle$ and $|\downarrow\rangle = |5S_{1/2}, F = 2, m_F = -1\rangle$. This necessitates two phase-coherent frequency components, which are provided by a system of two phase-locked diode lasers [29]. The laser fields are detuned by $-2\pi \times 9$ GHz relative to the single-photon transition to $|5P_{3/2}, F = 4\rangle$ while the frequency difference $\Delta_{|\uparrow\rangle|\downarrow\rangle}$ of the two components can be precisely set in the vicinity of the field-dependent transition frequency $\Delta_{|\uparrow\rangle|\downarrow\rangle}$ by a stable RF source. Figure 2(a) shows the magnetic-field dependence of the energy difference $\hbar\Delta_{|\uparrow\rangle|\downarrow\rangle}$ between both hyperfine states. Note that light shifts of the tweezer array and the spectroscopy beam modify $\Delta_{|\uparrow\rangle|\downarrow\rangle}$ [30]. The effective two-photon detuning

is given by $\delta_{\text{eff}} = \Delta_{12} - \Delta_{|\uparrow\rangle|\downarrow\rangle}$. For a beam radius of $w = 170(20) \mu\text{m}$ ($1/e^2$ waist) at the location of the array, we measure the on-resonance Rabi frequency ($\delta_{\text{eff}} = 0$) of $\Omega_{\text{R}} = 2\pi \times 0.6(1) \text{ MHz}$ over the 18×15 sites.

Figure 1(a) and Fig. 2(b) depict the magnetic-field geometry utilized for optical magnetometry in our individual-atom sensor grid. We apply a static homogeneous magnetic quantization field $|\mathbf{B}_{\text{q}}| = 283(1) \mu\text{T}$ induced by a pair of coils in Helmholtz configuration along the x-axis. This lifts the degeneracy of the magnetic hyperfine states and creates a well-defined quantization axis. Additionally, a pair of coils in anti-Helmholtz configuration allows for creation of a test gradient field \mathbf{B}_{t} .

A typical measurement cycle is visualized in Fig. 2(c). First, the occupation of atoms in the sensor grid is imaged. After activation of the quantization field, the state of the atoms is prepared in the measurement basis $\{|\uparrow\rangle, |\downarrow\rangle\}$. Without state preparation we find almost all of the atoms in state $|5S_{1/2}, F=3, m_F=-3\rangle$ which is not accessible to our Ramsey sequence. Via interrupted optical pumping using π -polarized laser light at the $|5S_{1/2}, F=3\rangle \rightarrow |5P_{3/2}, F=3\rangle$ transition in combination with repumping light at the $|5S_{1/2}, F=2\rangle \rightarrow |5P_{3/2}, F=3\rangle$ transition we can transfer about 30% of the atoms to $|\uparrow\rangle$. After state preparation, no atoms remain in $|\downarrow\rangle$ or other states of the $|5S_{1/2}, F=2\rangle$ manifold. Next, a Ramsey sequence with a $\pi/2$ -pulse of duration $\tau_{\pi/2} = 0.42 \mu\text{s}$ followed by a variable time T of free precession is initiated. After the second $\pi/2$ -pulse, atoms in $|\uparrow\rangle$ or any other states of the $|5S_{1/2}, F=3\rangle$ manifold are removed from the tweezer array and the magnetic field is switched off again. Finally, the remaining atoms in $|\downarrow\rangle$ are detected using fluorescence imaging.

In a sequence of measurement cycles, the periodic Ramsey signal is recorded by variation of T for a fixed differential two-photon energy $\hbar\Delta_{12}$ of the Ramsey spectroscopy beam (dashed horizontal line in Fig. 2(a)). The measured Ramsey frequency ω_{R} , given as 2π divided by the period of the Ramsey signal, directly corresponds to the effective detuning $\delta_{\text{eff}} = \Delta_{12} - \Delta_{|\uparrow\rangle|\downarrow\rangle} = \omega_{\text{R}}$. Accordingly, the differential shift of the basis states at the position of a sensor atom is revealed and can be translated into the magnetic-field strength using the field-dependence of the effective detuning of $\frac{\partial\delta_{\text{eff}}}{\partial B} = 2\pi \times 9.2777(3) \text{ kHz}/\mu\text{T}$.

In a first application, we use the 2D sensor grid to map the applied gradient test field \mathbf{B}_{t} depicted in Fig. 1(a) and Fig. 2(b). For this purpose, we execute a series of experimental cycles as illustrated in Fig. 2(c) recording the Ramsey signal for 55 equidistant steps of T within the interval of $2 \mu\text{s} \leq T \leq 110 \mu\text{s}$. For improved B -field resolution, we switch between cycles in which the gradient field (dashed blue) is activated or kept deactivated. The quantization field \mathbf{B}_{q} (pink) is activated in every cycle and data is collected in a pseudo-random way. All 270 sites in the sensor array are evaluated in parallel according to this procedure and detailed maps of the Ramsey frequencies for cycles with activated as well as deactivated test field are obtained. Both are pre-

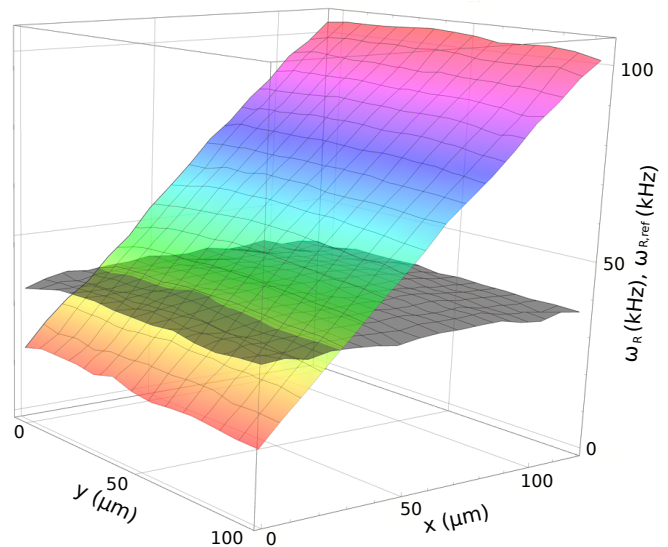


FIG. 3: Two-dimensional distribution of the Ramsey frequencies in the sensor plane without (gray) and with (color) activated magnetic gradient test field \mathbf{B}_{t} . A linear variation of ω_{R} along the x-direction is observed in case of an active test field while only fluctuations resulting from the local tweezer light shift in $\omega_{\text{R,ref}}$ occur for a deactivated test field.

sented in Fig. 3. Without test field, the whole sensor plane only shows slight variations due to the site-specific differential light shift of the tweezers. A nearly constant Ramsey frequency is measured with an average value of $\omega_{\text{R,ref}} = 2\pi \times 38.7(13) \text{ kHz}$. This corresponds to the preset frequency offset in Δ_{12} chosen to guarantee an adequate number of Ramsey oscillations within the measurement interval. The activation of the test field leads to a frequency map with a positive gradient along the quantization axis. There is an intersection of the two planes next to $x = 28 \mu\text{m}$ indicating almost no additional contribution of the test field to the transition energy $\hbar\Delta_{|\uparrow\rangle|\downarrow\rangle}$. A Ramsey frequency $\omega_{\text{R}} < \omega_{\text{R,ref}}$ shows that the test field reduces the effective magnetic field with respect to the reference measurement.

Based on the difference $\Delta\omega_{\text{R}} = \omega_{\text{R}} - \omega_{\text{R,ref}}$ between the Ramsey frequencies at each sensor pixel, the shift of the effective magnetic field strength $\Delta B = \frac{\partial B}{\partial \delta_{\text{eff}}} \times \Delta\omega_{\text{R}}$ resulting from the test field can be calculated for the whole sensor plane. The resulting field map is displayed in Fig. 4(a). The mean uncertainty of the frequency differences $\Delta\omega_{\text{R}}$ over the full area amounts to $2\pi \times 0.91(27) \text{ kHz}$ which calculates to a magnetic field resolution of $\delta B = 98(29) \text{ nT}$. We confirm this value by control measurements of $\omega_{\text{R,ref}}$ for small variations of the calibrated homogeneous quantization field \mathbf{B}_{q} in a 3×3 site measurement region (Fig. 1(c)). With increased data rates achieved by repeated assembly of atoms in this subarray [25], we are able to distinguish between magnetic

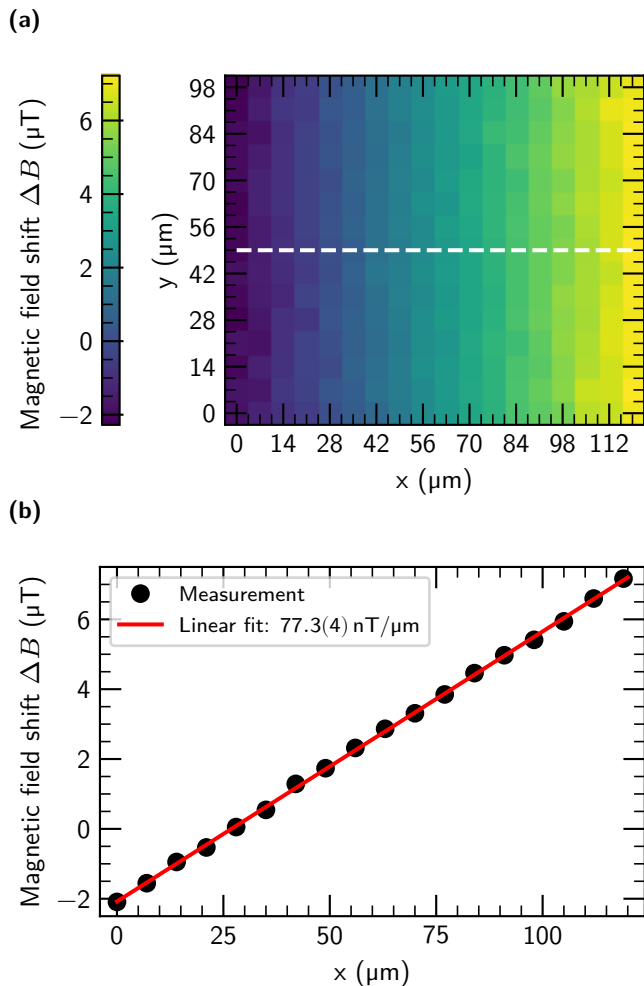


FIG. 4: Measured shift ΔB of the effective B-field strength. In the two-dimensional map (a), the results of the measurements for each of the 270 pixels equally distributed over the $119\ \mu\text{m} \times 98\ \mu\text{m}$ (18×15 pixel) sensor plane are given. The magnetic-field gradient along the x-direction is clearly visible. The data obtained along the dashed line are plotted in (b). From an approximation of a linear function (red) to this data, a gradient of $77.3(4)\ \text{nT}/\mu\text{m}$ is determined.

fields with minimum steps of $\simeq 100\ \text{nT}$.

Figure 4(b) gives the data along the dashed line ($y = 49\ \mu\text{m}$) in Fig. 4(a) and a linear fit (red) to the data. Based on values ranging from $-2.1(1)\ \mu\text{T}$ at $x = 0\ \mu\text{m}$ to $7.2(1)\ \mu\text{T}$ at $x = 119\ \mu\text{m}$, a gradient of $77.3(4)\ \text{nT}/\mu\text{m}$ is retrieved. Averaging over the set of gradients determined for the 15 rows gives a mean gradient of $76.9(7)\ \text{nT}/\mu\text{m}$ in the sensor area. Even though the test field exhibits a gradient along the y-direction as well, its contribution to the effective magnetic-field strength is below the resolution limit δB and therefore not observed when comparing measured data along y for constant x. This is consistent to a calculation based on the vector characteristics of the magnetic field and the measured gradient along x.

On average, only 719(200) atoms contribute to the measurement of the magnetic field at each sensor pixel. With an average time of free precession of $\bar{T} = 56\ \mu\text{s}$ per atom event, the total time of coherent evolution adds up to $\mathcal{T} = 40(11)\ \text{ms}$ which results in a sensitivity of $\delta B \times \sqrt{\mathcal{T}} = 20(7)\ \text{nT}/\sqrt{\text{Hz}}$. In laboratory time, the periods of atom preparation and detection have to be taken into account as well. Based on recent advances in repeated assembly of defect-free atom grids [25] and modular setups for separating atom preparation from the functional unit for sensing [28], a perpetual rate of 10 measurement cycles per second is achievable. Optimizing the Ramsey sequence by switching to states with maximum $|m_F|$ increases the susceptibility to magnetic fields by a factor of 2.5 and improves the resolution to $\delta B = 39(12)\ \text{nT}$. With both modifications, a B-field resolution below $10\ \text{nT}$ is accessible in our 2D sensor grid after one hour of laboratory time.

So far, spatial resolution has been limited to the geometric constraints of the array. While it enables parallelized detection at all sites of the sensing area and allows for creation of a detailed map of the field distribution at equidistant points, independent control of the specific positions is vital to enhance spatial resolution. Using the movable optical tweezer, the restriction to a periodic geometry can be surpassed and a single-atom scanning probe placed at any arbitrary position. Benchmarking this steerable probe with the known properties of the sensor grid, we obtain the same resolution in field strength and sensitivity. The spatial addressability is better than $100\ \text{nm}$, the spatial localization $< 1\ \mu\text{m}^2$ for a temperature of $52\ \mu\text{K}$ and trap depth of $U = k_B \times 0.2\ \text{mK}$, and the addressable area amounts to $400\ \mu\text{m} \times 400\ \mu\text{m}$ [27]. To summarize, in this work we have reported on the application of a tweezer array of individual atoms to quantum sensing. We experimentally demonstrated an optical magnetometer on the basis of a regular 2D sensor grid with micrometer-scale spacing which is built on a microlens-generated scalable optical tweezer architecture. The presented platform has been successfully benchmarked through the characterization of a gradient field with high resolution and sensitivity.

Already comprising hundreds of grid sites in this work, the scalability of the micro-optical approach enables the near-future implementation of 2D and - based on the Talbot effect - even 3D configurations of thousands of sensor pixels with adaptable geometry [26]. With bias fields and spectroscopy beams oriented along all three spatial coordinates, comprehensive mapping of external fields in a 3D volume can be achieved. Applications are not limited to magnetometry but can be extended to any external influence on atomic quantum states, e.g. the susceptibility of Rydberg states to electric fields. The use of microfabricated optical elements [31] facilitates the adaptation of the presented work to integrated setups, where we envision field-deployable atom-array quantum sensors. In addition to single-atom scanning, parallelized individual-atom scanning microscopy for quantum sensing can be

achieved by dynamic repositioning of the full sensor grid following the techniques demonstrated in Ref. [32]. Including a high-NA microscope objective and ground-state laser cooling bear the potential for superresolution imaging [33] of external fields with spatial resolution on the order of 100 nm and below in a parallelized fashion on the macroscopic sensor grid area. Finally, since our architecture is predestined for the implementation of collective quantum effects [27], next-generation protocols for quantum sensing exploiting superposition states and entanglement [5, 34–36] offer enticing prospects of quantum-enhanced order-of-magnitude improvements.

ACKNOWLEDGMENTS

We acknowledge financial support by the Federal Ministry of Education and Research (Grant No. 13N15981), by the Deutsche Forschungsgemeinschaft [Grants No. BI 647/6-1 and No. BI 647/6-2, Priority Program SPP 1929 (GiRyd)], and by the Open Access Publishing Fund of Technische Universität Darmstadt.

-
- [1] C. L. Degen, F. Reinhard, and P. Cappellaro, Quantum sensing, *Rev. Mod. Phys.* **89**, 035002 (2017).
- [2] M. W. Mitchell and S. Palacios Alvarez, Colloquium: Quantum limits to the energy resolution of magnetic field sensors, *Rev. Mod. Phys.* **92**, 021001 (2020).
- [3] D. Cohen, Magnetoencephalography: Detection of the Brain’s Electrical Activity with a Superconducting Magnetometer, *Science* **175**, 664 (1972).
- [4] D. Vasyukov, Y. Anahory, L. Embon, D. Halbertal, J. Cuppens, L. Neeman, A. Finkler, Y. Segev, Y. Myasoedov, M. L. Rappaport, M. E. Huber, and E. Zeldov, A scanning superconducting quantum interference device with single electron spin sensitivity, *Nature Nanotechnology* **8**, 639 (2013).
- [5] S. Danilin, A. V. Lebedev, A. Vepsäläinen, G. B. Lesovik, G. Blatter, and G. S. Paraoanu, Quantum-enhanced magnetometry by phase estimation algorithms with a single artificial atom, *npj Quantum Information* **4**, 1 (2018).
- [6] R. Stolz, M. Schiffler, M. Becken, A. Thiede, M. Schneider, G. Chubak, P. Marsden, A. B. Bergshjorth, M. Schaefer, and O. Terblanche, Squids for magnetic and electromagnetic methods in mineral exploration, *Mineral Economics* **35**, 467 (2022).
- [7] L. Rondin, J.-P. Tetienne, T. Hingant, J.-F. Roch, P. Maletinsky, and V. Jacques, Magnetometry with nitrogen-vacancy defects in diamond, *Reports on Progress in Physics* **77**, 056503 (2014).
- [8] J. F. Barry, J. M. Schloss, E. Bauch, M. J. Turner, C. A. Hart, L. M. Pham, and R. L. Walsworth, Sensitivity optimization for NV-diamond magnetometry, *Rev. Mod. Phys.* **92**, 015004 (2020).
- [9] S. C. Scholten, A. J. Healey, I. O. Robertson, G. J. Abrahams, D. A. Broadway, and J.-P. Tetienne, Widefield quantum microscopy with nitrogen-vacancy centers in diamond: Strengths, limitations, and prospects, *Journal of Applied Physics* **130**, 150902 (2021).
- [10] Z.-D. Zhang, S.-Y. Yin, L.-C. Wang, Y.-D. Wang, Y.-F. Li, Z.-N. Tian, and Q.-D. Chen, Single NV centers array preparation and static magnetic field detection, *Opt. Express* **30**, 32355 (2022).
- [11] D. Budker and M. Romalis, Optical magnetometry, *Nature Physics* **3**, 227 (2007).
- [12] J. Kitching, Chip-scale atomic devices, *Applied Physics Reviews* **5**, 031302 (2018).
- [13] L. Amico, M. Boshier, G. Birkl, A. Minguzzi, C. Miniatura, L.-C. Kwek, D. Aghamalyan, V. Ahufinger, D. Anderson, N. Andrei, A. S. Arnold, M. Baker, T. A. Bell, T. Bland, J. P. Brantut, D. Cassettari, W. J. Chetcuti, F. Chevy, R. Citro, S. De Palo, R. Dumke, M. Edwards, R. Folman, J. Fortagh, S. A. Gardiner, B. M. Garraway, G. Gauthier, A. Günther, T. Haug, C. Hufnagel, M. Keil, P. Ireland, M. Lebrat, W. Li, L. Longchambon, J. Mompert, O. Morsch, P. Naldesi, T. W. Neely, M. Olshanii, E. Orignac, S. Pandey, A. Pérez-Obiol, H. Perrin, L. Piroli, J. Polo, A. L. Pritchard, N. P. Proukakis, C. Rylands, H. Rubinsztein-Dunlop, F. Scazza, S. Stringari, F. Tosto, A. Trombettoni, N. Victorin, W. v. Klitzing, D. Wilkowski, K. Khani, and A. Yakimenko, Roadmap on atomtronics: State of the art and perspective, *AVS Quantum Science* **3**, 039201 (2021).
- [14] S. Aigner, L. D. Pietra, Y. Japha, O. Entin-Wohlman, T. David, R. Salem, R. Folman, and J. Schmiedmayer, Long-range order in electronic transport through disordered metal films, *Science* **319**, 1226 (2008).
- [15] F. Yang, A. J. Kollár, S. F. Taylor, R. W. Turner, and B. L. Lev, Scanning quantum cryogenic atom microscope, *Phys. Rev. Appl.* **7**, 034026 (2017).
- [16] M. Vengalattore, J. M. Higbie, S. R. Leslie, J. Guzman, L. E. Sadler, and D. M. Stamper-Kurn, High-resolution magnetometry with a spinor Bose-Einstein condensate, *Phys. Rev. Lett.* **98**, 200801 (2007).
- [17] H. B. Dang, A. C. Maloof, and M. V. Romalis, Ultrahigh sensitivity magnetic field and magnetization measurements with an atomic magnetometer, *Applied Physics Letters* **97**, 151110 (2010).
- [18] Y. Eto, H. Ikeda, H. Suzuki, S. Hasegawa, Y. Tomiyama, S. Sekine, M. Sadgrove, and T. Hirano, Spin-echo-based magnetometry with spinor Bose-Einstein condensates, *Phys. Rev. A* **88**, 031602 (2013).
- [19] O. Eliasson, R. Heck, J. S. Laustsen, M. Napolitano, R. Müller, M. G. Bason, J. J. Arlt, and J. F. Sherson, Spatially-selective in situ magnetometry of ultracold atomic clouds, *Journal of Physics B: Atomic, Molecular and Optical Physics* **52**, 075003 (2019).
- [20] R. J. Sewell, M. Koschorreck, M. Napolitano, B. Dubost, N. Behbood, and M. W. Mitchell, Magnetic sensitivity beyond the projection noise limit by spin squeezing, *Phys. Rev. Lett.* **109**, 253605 (2012).
- [21] W. Muessel, H. Strobel, D. Linnemann, D. B. Hume, and M. K. Oberthaler, Scalable spin squeezing for quantum-enhanced magnetometry with bose-einstein condensates, *Phys. Rev. Lett.* **113**, 103004 (2014).

- [22] K. Singh, C. E. Bradley, S. Anand, V. Ramesh, R. White, and H. Bernien, Mid-circuit correction of correlated phase errors using an array of spectator qubits, *Science* **380**, 1265 (2023).
- [23] A. M. Kaufman and K.-K. Ni, Quantum science with optical tweezer arrays of ultracold atoms and molecules, *Nature Phys* **17**, 1324 (2021).
- [24] R. Dumke, M. Volk, T. Mütther, F. B. J. Buchkremer, G. Birkel, and W. Ertmer, Micro-optical Realization of Arrays of Selectively Addressable Dipole Traps: A Scalable Configuration for Quantum Computation with Atomic Qubits, *Phys. Rev. Lett.* **89**, 097903 (2002).
- [25] D. Ohl de Mello, D. Schäffner, J. Werkmann, T. Preuschoff, L. Kohfahl, M. Schlosser, and G. Birkel, Defect-Free Assembly of 2D Clusters of More Than 100 Single-Atom Quantum Systems, *Phys. Rev. Lett.* **122**, 203601 (2019).
- [26] M. Schlosser, S. Tichelmann, D. Schäffner, D. Ohl de Mello, M. Hambach, J. Schütz, and G. Birkel, Scalable multilayer architecture of assembled single-atom qubit arrays in a three-dimensional Talbot tweezer lattice, *Phys. Rev. Lett.* **130**, 180601 (2023).
- [27] M. Schlosser, D. Ohl de Mello, D. Schäffner, T. Preuschoff, L. Kohfahl, and G. Birkel, Assembled arrays of Rydberg-interacting atoms, *Journal of Physics B: Atomic, Molecular and Optical Physics* **53**, 144001 (2020).
- [28] L. Pause, T. Preuschoff, D. Schäffner, M. Schlosser, and G. Birkel, Reservoir-based deterministic loading of single-atom tweezer arrays (2023), arXiv:2302.12730.
- [29] T. Preuschoff, P. Baus, M. Schlosser, and G. Birkel, Wide-band current modulation of diode lasers for frequency stabilization, *Review of Scientific Instruments* **93**, 063002 (2022).
- [30] G. Ramola, R. Winkelmann, K. Chandrashekhara, W. Alt, P. Xu, D. Meschede, and A. Alberti, Ramsey imaging of optical traps, *Phys. Rev. Applied* **16**, 024041 (2021).
- [31] G. Birkel, F. Buchkremer, R. Dumke, and W. Ertmer, Atom optics with microfabricated optical elements, *Optics Communications* **191**, 67 (2001).
- [32] A. Lengwenus, J. Kruse, M. Schlosser, S. Tichelmann, and G. Birkel, Coherent Transport of Atomic Quantum States in a Scalable Shift Register, *Phys. Rev. Lett.* **105**, 170502 (2010).
- [33] E. Deist, J. A. Gerber, Y.-H. Lu, J. Zeiher, and D. M. Stamper-Kurn, Superresolution microscopy of optical fields using tweezer-trapped single atoms, *Phys. Rev. Lett.* **128**, 083201 (2022).
- [34] T. Ruster, H. Kaufmann, M. A. Luda, V. Kaushal, C. T. Schmiegelow, F. Schmidt-Kaler, and U. G. Poschinger, Entanglement-based dc magnetometry with separated ions, *Phys. Rev. X* **7**, 031050 (2017).
- [35] E. Dietsche, A. Larrouy, S. Haroche, J. Raimond, M. Brune, and S. Gleyzes, High-sensitivity magnetometry with a single atom in a superposition of two circular Rydberg states, *Nature Physics* **15**, 326 (2019).
- [36] P. Sekatski, S. Wölk, and W. Dür, Optimal distributed sensing in noisy environments, *Phys. Rev. Research* **2**, 023052 (2020).